Flexible and Stretchable Fiber-Shaped Triboelectric Nanogenerators for Biomechanical Monitoring and Human-Interactive Sensing

Chuan Ning, Kai Dong, Renwei Cheng, Jia Yi, Cuiying Ye, Xiao Peng, Feifan Sheng, Yang Jiang, and Zhong Lin Wang*

Wearable, flexible, and even stretchable tactile sensors, such as various types of electronic skin, have attracted extensive attention, which can adapt to complex and irregular surfaces, maximize the matching of wearable devices, and conformally apply onto human organs. However, it is a great challenge to simultaneously achieve breathability, permeability, and comfortability for their development. Herein, mitigating the problem by miniaturizing and integrating the sensors is tried. Highly flexible and stretchable coaxial structure fiber-shaped triboelectric nanogenerators (F-TENGs) with a diameter of 0.63 mm are created by orderly depositing conductive material of silver nanowires/carbon nanotubes and encapsulated polydimethylsiloxane onto the stretchable spandex fiber. As a self-powered multifunctional sensor, the resulting composite fiber can convert mechanical stimuli into electrical signals without affecting the normal human body. Moreover, the F-TENGs can be easily integrated into traditional textiles to form tactile sensor arrays. Through the tactile sensor arrays, the real-time tactile trajectory and pressure distribution can be precisely mapped. This work may provide a new method to fabricate fiber-based pressure sensors with high sensitivity and stretchability, which have great application prospects in personal healthcare monitoring and human–machine interactions.

1. Introduction

Wearable tactile sensors are an important element of medical wisdom, robot technology, human–machine interfaces, and artificial intelligence technology (AIT).[1–3] There have been many research reports to develop various wearable tactile sensors, for example, various types of electronic skin.[4–6] Such kinds of tactile sensors can adapt to irregular surfaces[7,8] and conformally apply on human organs aiming at collecting human physical data for personal healthcare monitoring[9–11] or human-interactive sensing.[12–14] However, it is difficult for traditional electronic skin to simultaneously satisfy the demands for breathability, permeability, and comfortability.[15–18] Considering the human skin is able to excrete secretions from sebaceous glands and sweat from sweat glands through pores, electronic skin also needs the ability to exchange gas and water with external environment.[19,20] One straightforward method is to create holes in electronic skins, but recklessly creating holes in electronic skins will weaken their toughness. An effective method is to miniaturize the blocky tactile sensors and integrate the miniaturized sensors by the knitting process.[21,22]

Triboelectric nanogenerators (TENGs) are a kind of technology that can convert mechanical energy into electricity based on the coupling effect of triboelectrification and electrostatic induction.[23–25] As a new energy harvesting method, TENGs have many advantages, such as light weight, low cost, versatile material selection, and simple structure design.[26–28] In addition, the coaxial structure has been widely applied for fiber-shaped supercapacitors,[29–31] lithium batteries,[32] and solar cells.[33–34] And the coaxial structure shows a higher stability under various mechanical deformations, especially bending and stretching.[30,35] Therefore, the coaxial structure can be used to fabricate fiber-shaped triboelectric nanogenerators (F-TENGs). The F-TENGs could be integrated with human body without affecting the normal human body or woven into fabrics as a tactile sensor array.[36–38] Both the single F-TENG and the tactile sensor arrays can meet the human body's need for breathability, permeability, and comfortability, which can replace for conventional sensors and

C. Ning, Prof. K. Dong, R. Cheng, J. Yi, C. Ye, X. Peng, F. Sheng, Y. Jiang,
Prof. Z. L. Wang
CAS Center for Excellence in Nanoscience
Beijing Key Laboratory of Micro-Nano Energy and Sensor
Beijing Institute of Nanoenergy and Nanosystems
Chinese Academy of Sciences
Beijing 100083, China
E-mail: zhong.wang@mse.gatech.edu
C. Ning, Prof. K. Dong, R. Cheng, C. Ye, X. Peng, Y. Jiang,
Prof. Z. L. Wang
School of Nanoscience and Technology
University of Chinese Academy of Sciences
Beijing 100049, China
J. Yi, F. Sheng
Center on Nanoenergy Research
School of Physical Science and Technology
Guangxi University
Nanning 530004, China
Prof. Z. L. Wang
School of Material Science and Engineering
Georgia Institute of Technology
Atlanta, GA 30332, USA

provide more opportunities for breathable, comfortable, and wearable sensors.

Herein, a highly flexible and stretchable coaxial structure F-TENG with a diameter of 0.63 mm is fabricated by successively depositing conductive material of silver nanowires (Ag NWs)/carbon nanotubes (CNTs) and encapsulated material of polydimethylsiloxane (PDMS) onto the surface of a stretchable spandex fiber. As self-powered tactile sensors, the F-TENGs are capable of converting mechanical energy into electricity and responding to versatile mechanical stimuli. The F-TENGs with good flexibility and excellent mechanical stability are composed of stretchable components, which can achieve over 140% strain. Therefore, they can fully conform on movable objects, irregular objects, and organs to record the number of steps, recognize different gestures, and the bending angles of the fingers without affecting the normal human body. Furthermore, due to its excellent mechanical properties, it could also be integrated into traditional textiles. A tactile sensor array with 8 × 8 pixels is woven based on the F-TENGs as a tactile sensor and human–machine interface, through which we can detect the real-time pressure distribution and recognize the touching positions. The tactile sensors are able to achieve breathability, air permeability, and comfortability, which make a contribution to the practical sensing platform.

2. Results and Discussion

Recently, various kinds of F-TENGs have been made by different methods. However, some of them have complex methods, and some have large diameters or cannot be stretched, as shown in Table S1 in the Supporting Information. The stretchable F-TENGs with a diameter of 0.63 mm are fabricated by a three-step coating method. **Figure 1**a schematically shows the details of the production process. The Ag NWs are first deposited onto a stretchable spandex fiber substrate. To further enhance
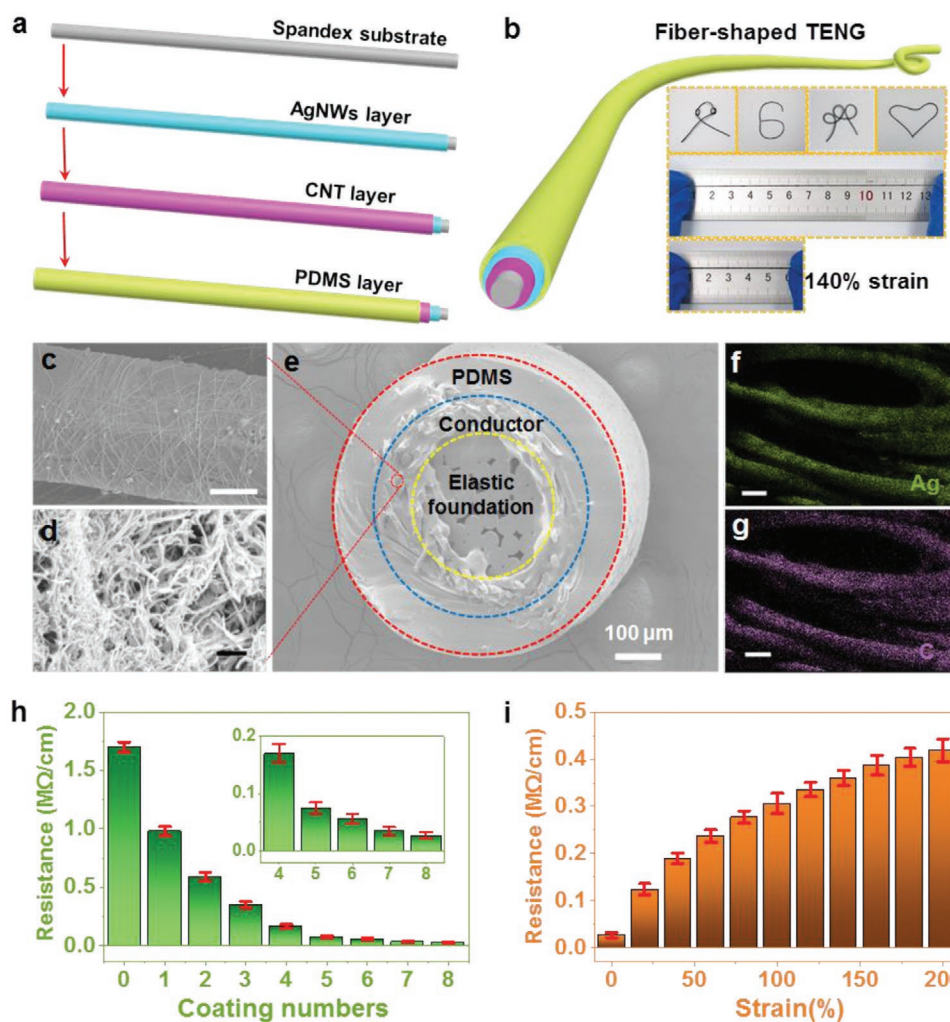

Figure 1. Fabrication process, device structure, and electrical conductivity of the F-TENGs. a) The preparation process of the F-TENGs. b) Schematic diagram and photographs of the flexible and stretchable F-TENG. The F-TENGs can be well maintained after being stretched with a strain up to 140%, and can also be folded into different shapes. SEM images of c) Ag NWs electrode (scale bar: 5 µm) and d) CNTs electrode (scale bar: 500 nm) coated on the spandex fiber. e) Cross-sectional SEM view of the F-TENGs. Energy dispersive spectroscopy mapping of f) carbon and g) silver element, respectively (scale bar: 20 µm). h) The electric resistance of the conductive fiber changes with the number of soaking–drying cycle operation. i) The electric resistance changes of the F-TENG with the initial length of 100 mm at various strain levels (0–200%).

**ADVANCED
SCIENCE NEWS**

www.advancedsciencenews.com

**ADVANCED
FUNCTIONAL
MATERIALS**

www.afm-journal.de

the conductivity and stability, CNT solution is then dip coated onto the as-prepared fiber. The CNT covers the surfaces of Ag NWs as well as the gap between them. The composite fiber is subsequently encapsulated by PDMS to form the coaxial structure. Figure 1b shows the schematic diagram and photographs of the fabricated F-TENGs. As shown in the inset of Figure 1b, the F-TENGs could stay intact after stretching with a strain up to 140%, which could also be knotted and folded into various shapes, such as the number six, a kite, and a heart. It can be found that the F-TENGs have excellent stretchability and flexibility, which can adapt to irregular surfaces and conformally apply on human organs even be woven into textiles. As illustrated in Figure 1e, the cross-sectional scanning electron microscopy (SEM) image of the F-TENG held a clear core–sheath structure. Red, yellow, and blue dashed lines outline the cross-section of the F-TENG, stretchable spandex fiber substrate, and conducting layer, respectively. CNT/Ag NWs composite conducting layer is sandwiched between the inner substrate and outer PDMS. As depicted in Figure S1 in the Supporting Information, the diameters of the F-TENGs are measured by a thickness tester, which is about 0.63 mm. As shown in Figure S3 in the Supporting Information, the F-TENGs have a small diameter and excellent flexibility, which can be fabricated into most fabrics. Figure 1c,d shows the SEM images of Ag NWs and CNTs coating, indicating the rough and porous structure. From the SEM images, many inter-crossed Ag NWs with the range of diameters about tens of micrometers can be observed. The CNTs with the size from 2–5 μm cover the surfaces of Ag NWs as well as the gap between them. As shown in Figure S2 in the Supporting Information, Ag NWs and CNTs cross with each other and form a tree-shaped conducting layer (Ag NWs as the backbone and CNTs as the branches), which are uniformly dip coated onto the stretchable spandex fiber substrate. The tree-shaped conducting layer not only helps to enhance the conductivity and mechanical stability but also provides an enhanced elasticity. Figure 1f,g shows the energy dispersive spectrometer (EDS) images of the F-TENG, and Figure S4 in the Supporting Information shows the corresponding SEM images, through which we can further understand the distribution of the conductive materials in the conducting layer. To further explore the electrical conductivity of stretchable conductive fibers, the changes in electric resistance of the fiber is studied. As depicted in Figure 1h, the nonconductive spandex fiber becomes conductive when the Ag NWs are first deposited onto it. CNT solution is then repeatedly dip coated onto the as-prepared fiber. As shown in Figure 1h, the electric resistance of the conductive fiber gradual decline with the increase of the number of soaking–drying cycles, and the reductions flattens out. In addition, as a stretchable fiber, elongation is an important factor affecting the electric resistance. From Figure 1i, we can see higher electric resistance of conductive fiber is produced when the strain level is higher because when the fiber was stretched, the conducting material became loose, as shown in Figure S5 in the Supporting Information.

The operating principle of the F-TENGs is briefly demonstrated in **Figure 2**a, which involves a conjunction of contact electrification and electrostatic induction.[39] In the original position, an active object having a lower electron affinity contacts with the surfaces of the PDMS. Because of the opposite triboelectric polarities of active object and PDMS, the equivalent negative and positive electrostatic charges will be generated at the two contact surfaces (Figure 2a,i). Once the two surfaces are moving away from each other, the electric potential of electrode layer will rise and prompt electrons to flow to the ground, resulting in an electrical current (Figure 2a,ii). When the gap between two triboelectric-charged surfaces increases, a new equilibrium state can be established and the electrons will stop moving (Figure 2a,iii). As the object approaches to the PDMS again, the electrons will flow from the ground to electrode layer to make a charge balance (Figure 2a,iv). When the active object fully contacts with the PDMS again, no electrical output can be observed. This is the entire working cycle of the F-TENGs. To support the proposed mechanism of the electricity generating process, the electric potential between the Cu film and the PDMS is simulated by using the COMSOL software (Figure 2b).

To characterize the output performance of the F-TENGs, a measurement platform is established. A F-TENG with the length of 5 cm is fixed to an acrylic panel, while a piece of Cu film is attached to another acrylic panel, which is attached to the vibrating surface of a linear motor. When the linear motor works, the Cu film will regularly contact with the F-TENG. The open-circuit voltage (V_{OC}), short-circuit current (I_{SC}), and short-circuit charge transfer (Q_{SC}) are measured under the frequencies ranging from 1 to 5 Hz. As shown in Figure 2c–e, the V_{OC} and Q_{SC} are nearly stable, approaching to 22 V and 7.5 nC, respectively. At the same time, higher impact frequency generates higher I_{SC}. The obtained I_{SC} can reach 0.6 μA at the frequency of 5 Hz. Figure S6a–c in the Supporting Information presents the details of V_{OC}, I_{SC}, and Q_{SC} under the operating frequency of 1 Hz and the compressing force of 20 N. The output power density is also measured by externally connecting different loads from 10 kΩ to 3 GΩ under the tapping frequency of 1 Hz. As displayed in Figure 2f, when the loading resistance is below 10 MΩ, the output voltage and current reveal no notable variation. As the load resistance increased from 10 MΩ to 1 GΩ, the output voltage increased while the output current decreased. The maximum output power density is 21.5 μW m^{-1} at a load resistance of 150 MΩ (Figure 2g). In addition, the stability of the F-TENG is tested through continuously tapping it for 30 min. As shown in Figure 2h and Figure S7 in the Supporting Information, the I_{SC} and V_{OC} stably sustains about 0.2 μA and 22 V, respectively. The insets exhibit the detailed I_{SC} and V_{OC} of the early five cycles and the last five cycles, respectively. Moreover, washability is also a necessary requirement for wearable tactile sensors. In this study, the domestic washing environment is developed with a magnetic stirrer, as shown in Figure S8a in the Supporting Information. The F-TENGs are agitated in a beaker with water and detergent by a magnetic stirrer for laundering of 20 min. Figure S8b in the Supporting Information shows that the V_{OC} of the F-TENGs have no obvious degradation after multiple detergent washing. Figure S9 in the Supporting Information shows the SEM images of F-TENG before and after wash. As we can see, the F-TENG has no obvious change after detergent washing. This indicates that the F-TENGs have excellent washability.

When an F-TENG is stretched under various tensile strains, a Cu film is attached to the linear motor that can
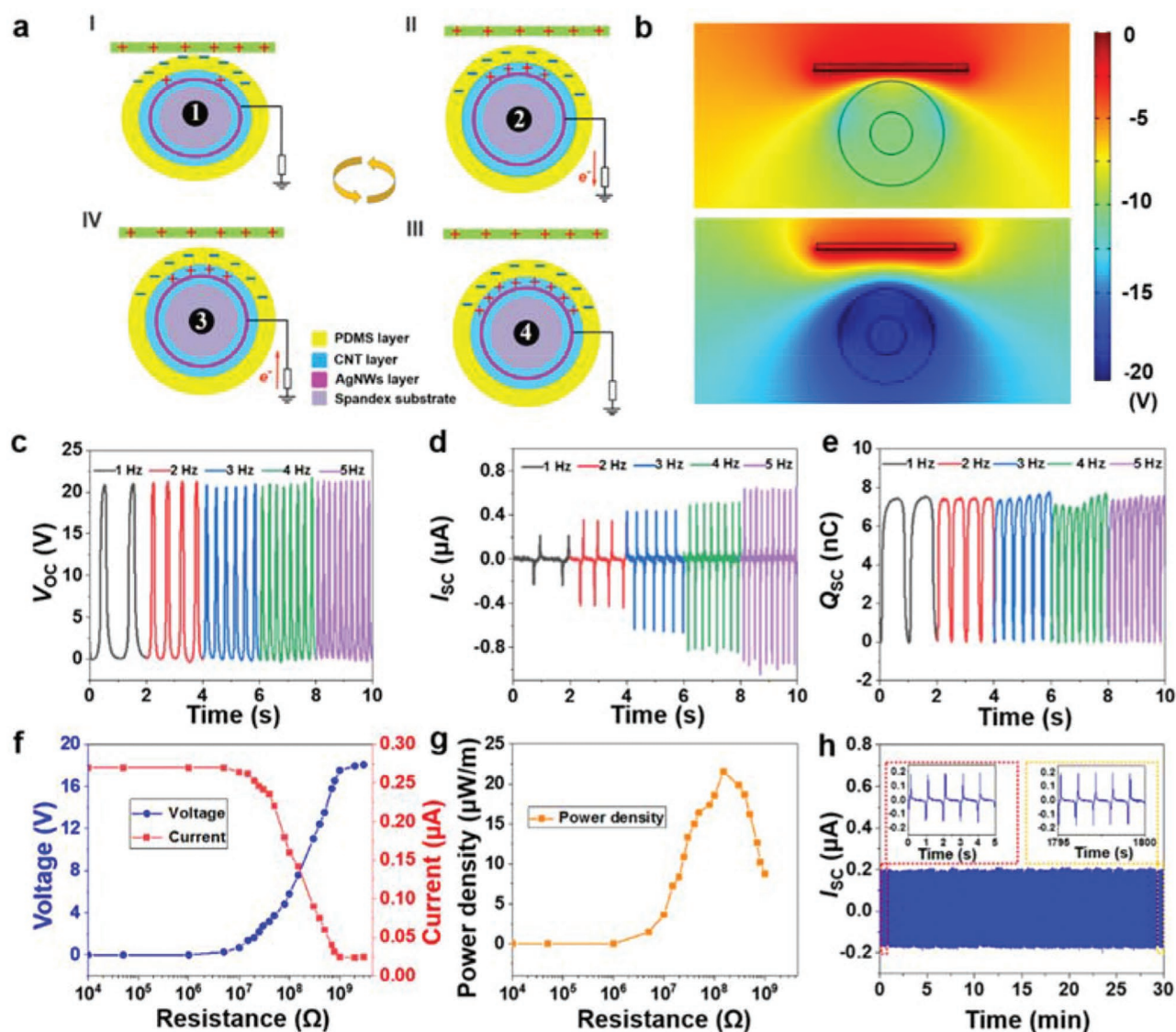
Figure 2. Working mechanism and electrical output performance of the F-TENGs. a) Schematic diagrams showing the working principle of the F-TENGs. b) Numerical calculation of the corresponding electrical potential distribution by the COMSOL software. c) V_{OC}, d) I_{SC}, and e) Q_{SC} of the F-TENGs under different frequencies (1–5 Hz). f) The variation of voltage and current and g) power density of the F-TENGs with different external load resistance. h) Stability test of the F-TENGs under continuous impact for 30 min. The insets exhibit the detailed I_{SC} of the early five cycles and the last five cycles.

regularly contact with the F-TENG under the operating frequency of 1 Hz. Here, the tensile strain is defined as $\varepsilon = (d - d_0)/d_0 \times 100\%$, where d is the elongated length and d_0 is the original length. As shown in **Figure 3**a–c, electrical outputs decreased linearly with the increment of tensile strains from 20% to 140%. The V_{OC} decreased from 22 to 12 V, and the corresponding I_{SC} decreased from 0.21 to 0.12 µA. The Q_{SC} also decreased from 7.4 to 4.7 nC. The reason could be that when the F-TENG was stretched, the conducting layer of the F-TENGs became loose and the resistance increased as the F-TENG was stretched. In addition, the diameter of the F-TENGs decrease and the decrease of diameter brings less contact area with the outside substrate as the F-TENG was stretched.

To investigate the effect of diameters on the electrical output performances, the F-TENGs with different diameters are fabricated (Figure 3g). The sizes of diameters are determined by the thickness of PDMS deposited onto the outermost layer. The operating frequency is controlled as 1 Hz and the magnitude of the external force is 20 N. The electric outputs of the F-TENGs decrease with the increasing of the diameter (Figure 3d–f). More increase in diameter would lead to the reduction of power output due to the reduced electrostatic induction effect. The stretchability of the F-TENGs under different diameters is systematically studied. The strain–tension curves are shown in Figure 3h. The increased diameter of the F-TENGs will increase the tension, while the F-TENGs with smaller diameters can provide greater elongation. Furthermore, F-TENGs
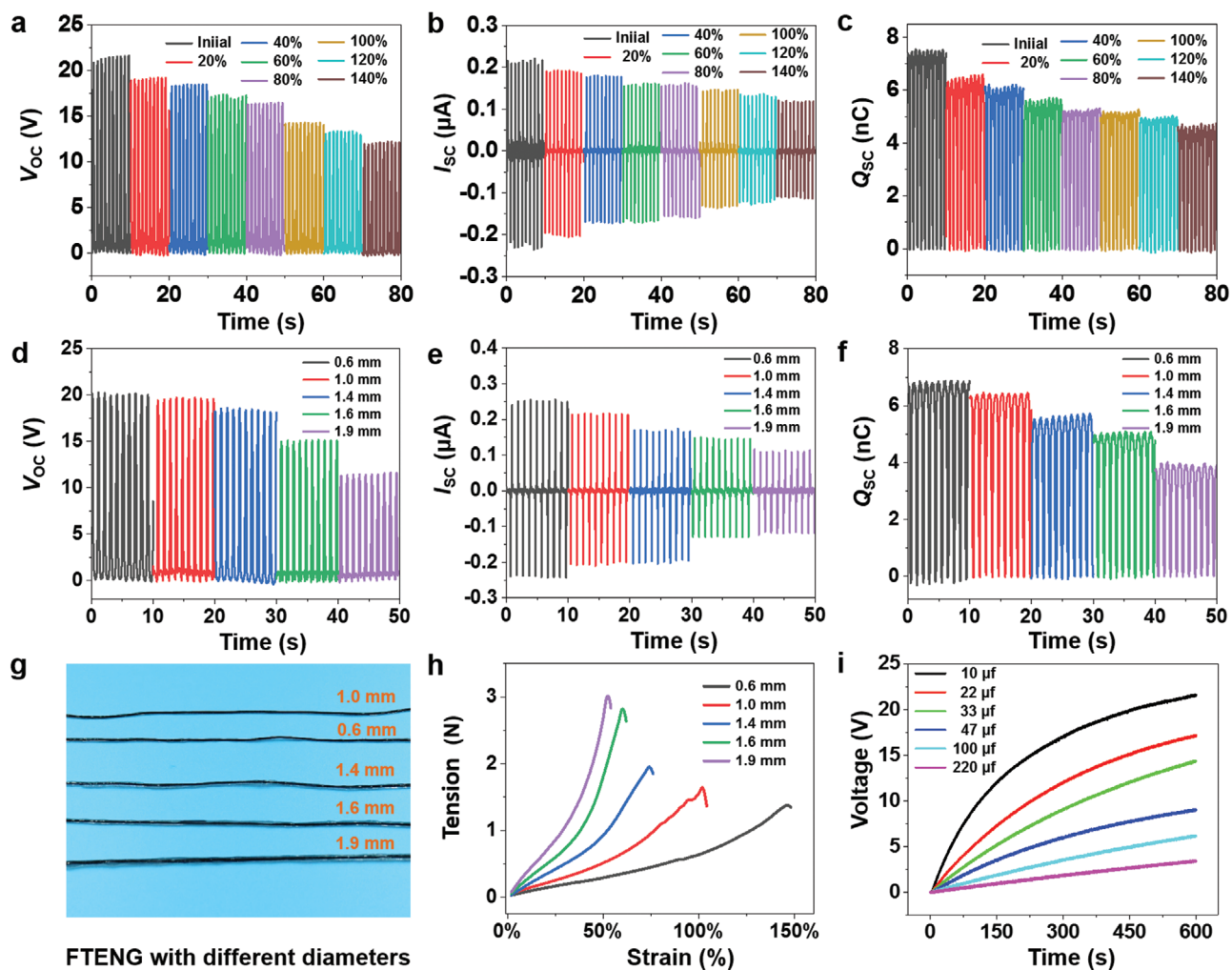
**ADVANCED
SCIENCE NEWS**

www.advancedsciencenews.com

**ADVANCED
FUNCTIONAL
MATERIALS**

www.afm-journal.de

Figure 3. Effects of tensile strain and diameter on the electrical output and mechanical properties of the F-TENGs. a) V_{OC}, b) I_{SC}, and c) Q_{SC} of the F-TENGs at various tensile strain levels (20–140%). The initial length is 50 mm and the contact frequency is 1 Hz. d) V_{OC}, e) I_{SC}, and f) Q_{SC} of the F-TENGs under different diameters. g) The photo of the F-TENGs fabricated with different diameters. h) The strain–tension curves of the F-TENGs under different diameters. i) Charging curves of the F-TENGs under different capacitance capacities.

have no significant change except a slight decrease in diameter after stretching to 80% for 100 cycles, as shown in Figure S10 in the Supporting Information. The electricity generated from the F-TENGs can be further stored in commercial capacitors. The alternating current (AC) output of the F-TENGs can be converted to direct current (DC) output through the bridge circuit. Figure 3i exhibits the charging process of different capacitors (10, 22, 33, 47, 100, and 220 μF) under the impact frequency of 5 Hz, which shows that the F-TENGs can be used to charge the capacitors, but the charging velocity is decreased with the increasing of capacitance.

To study the pressure sensitivity of the F-TENGs, the relationship between electrical output and the loading forces is studied. As shown in **Figure 4**a, V_{OC} and I_{SC} increase with the increasing of the loading forces. Under the tapping force of 1 N, the maximum Voc and Isc generated by the F-TENG are 10 V and 0.1 μA, respectively. When the force increases to 45 N, the V_{OC} and I_{SC} reach to 24.5 V and 0.21 μA, respectively. As shown in Figure S11 in the Supporting Information, the con-

ductive materials are loose and cannot fully contact with each other under a small loading force. The contact area increases between the conductive materials and the resistance decreases with the increasing of the loading force, which can improve the sensitivity of the F-TENG. The sensitivity of the tactile sensor is shown in Figure S12 in the Supporting Information. When the tapping force is less than 4 kPa the sensitive of the tactile sensor can reach 5.2 mV Pa^{-1}, when the force is greater than 4 kPa the sensitive is 0.39 mV Pa^{-1}. Figure S13 in the Supporting Information shows the details of V_{OC} and I_{SC} of the F-TENG with different applied loadings (5, 10, 15, 20, 30, and 40 N). Based on the excellent flexibility and high sensing features of the F-TENGs, a self-powered human motion detector is developed. Because the heel can maximally contact with the ground, an F-TENG is sewn on the heel of a sock. As demonstrated in Figure 4b, when the tester walks or runs, the periodic contact separation between the feet and the ground generates periodic electrical signals. Furthermore, the course of running the heel contacts more fully with the ground, resulting in a
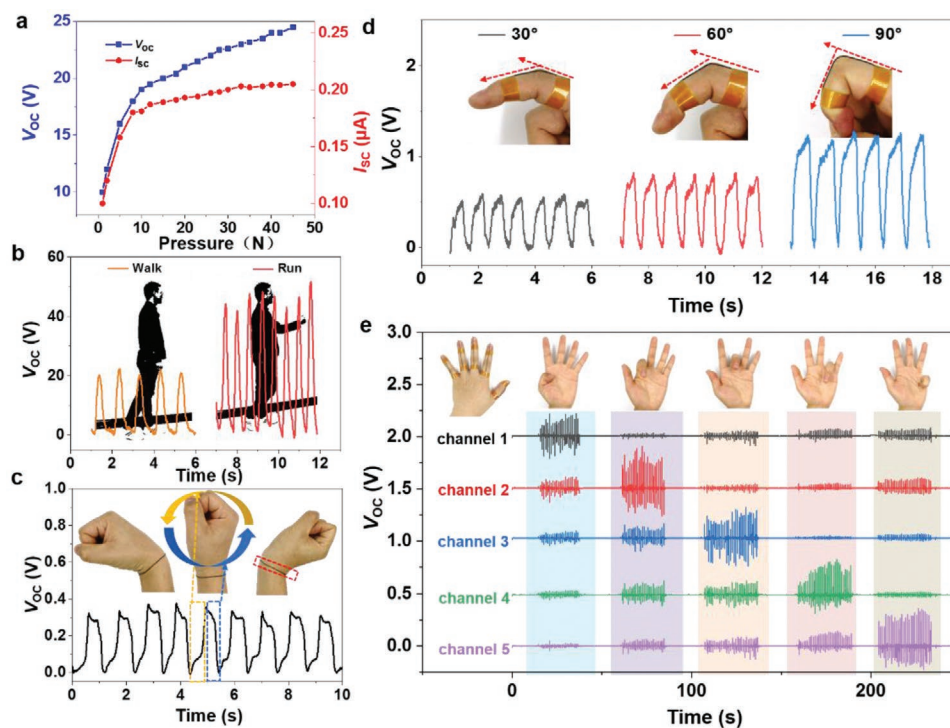
Figure 4. Sensing features and physiological monitoring application of the F-TENGs. a) Variations of V_{OC} and I_{SC} of the F-TENGs as a function of loading force. b) Voltage signals of an F-TENG attached on foot when the personal is walking and running. The insets exhibit the different motion states of the personal, including walking and running. c) Real-time voltage outputs of an F-TENG for monitoring various motion states of the wrist. Inset is a movement track of the wrist with an F-TENG. d) The peak value of voltage of an F-TENG under different bending angles of the finger, including 30°, 60°, and 90°. The insets are schematics of the F-TENGs fixed on the finger. e) Voltage output signals of the five F-TENGs that are fixed on the five fingers from the thumb to the little finger. Inset is the photograph of a hand with five F-TENGs fixed on its fingers.

higher electrical output. According to these electrical signals, we can understand the movement behaviors of the human body and record the number of steps. Furthermore, an F-TENG is mounted on a wrist of the tester. When the wrist is bent, the F-TENG is stretched to contact with or separate from the skin (Figure 4c). Figure S14a in the Supporting Information shows the motion trajectory of the wrist. The F-TENG is compressed and voltage output increases from 0 to 0.35 V when the wrist is bent inward. And the voltage output falls to zero with the release of the wrist, as shown in Figure S14b in the Supporting Information. Therefore, each output cycle corresponds to one bending cycle of the wrist.

The F-TENGs can also monitor the motions of the hands. An F-TENG is attached to a finger for monitoring its bending amplitude. Figure 4d shows the voltage output of the tactile sensors under different bending angles (from 30°, 60° to 90°). The corresponding voltage output shows a linear increase with the increasing of the bending angles, which may be attributed to the larger contact pressure between the F-TENG and the skin under larger bending angle. Meanwhile, the outputs of different cycles for each bending angle show excellent repeatability. In other words, there is a stable relationship between the electrical output performance and the bending angles. Five F-TENGs are fixed on the five fingers to further demonstrate the feasibility for the recognition of hand gestures (Figure 4e). Some interferences can be attributed to the movement of one finger making other fingers show slight resonant reactions.

However, the output voltages of the finger under the bending state are clearly higher than those under the oscillatory states. Moreover, different gesticulations can also be judged by a smart glove. Five F-TENGs connected in parallel are integrated into five fingers of a smart glove, as shown in the Figure S15a in the Supporting Information. Wearing the smart glove can produce corresponding electric signals according to various gestures. As illustrated in the left of Figure S15b in the Supporting Information, the voltage outputs of the smart glove will record the various gestures of the tester, including the victory sign, the "OK" gesture, the gesture of the number four, and the act of making a fist. The corresponding detailed electric signals are shown in the right of Figure S15b in the Supporting Information. Through the above research, the F-TENGs can be used to monitor the motions of the human body, which have potential applications for robotics or intelligent prosthetics.

In order to realize the practical applications of intelligent human–machine interactions,[40] robotics,[41] and movement monitoring,[27] the capabilities of recognizing the tactile trajectory and detecting the pressure distribution are one of the key techniques. There are some reports to realize the techniques through the electronic skin. However, traditional electronic skin has poor breathability, permeability, and comfortability. To this end, the F-TENG-based tactile sensor arrays are fabricated. **Figure 5**a exhibits an F-TENG-based tactile sensor array with 8×8 pixels. The sensory pixels are formed by the overlapped area in each weft yarn and warp yarn. As shown in the inset of

ADVANCED
SCIENCE NEWS
www.advancedsciencenews.com

ADVANCED
FUNCTIONAL
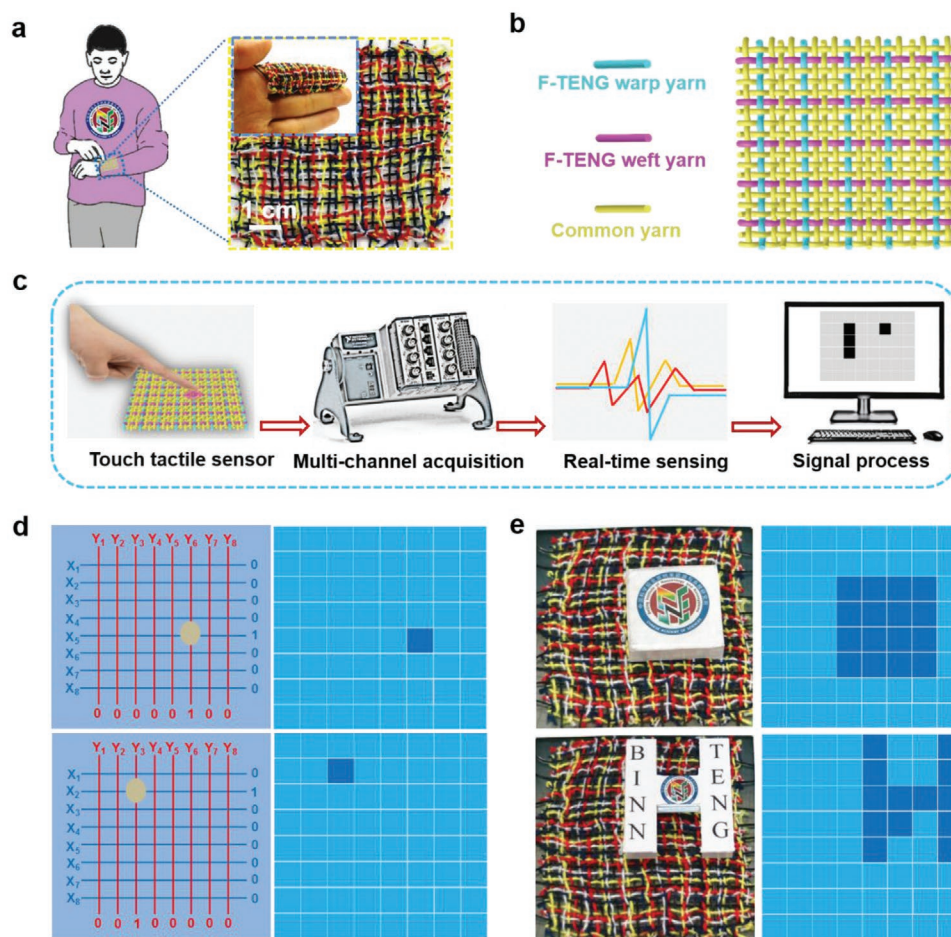**MATERIALS**
www.afm-journal.de

Figure 5. Fabrication and application of the F-TENG-based tactile sensor arrays. a) Structural representation of the F-TENG-based tactile sensor arrays. b) The photograph of an F-TENG-based tactile sensor array with the dimension of 70×70 mm². Inset is the index finger that is wrapped conformally by the tactile sensor array. c) Schematic diagram of the operation of the tactile sensor arrays for real-time pressure tracking, which includes a F-TENG-based tactile sensor array, a voltage measurement device, real-time output voltage of each sensor unit, and the specialized developed data analysis and processing software. d) The finger touching positions displayed through reading the color changes. e) Photographs of an F-TENG-based tactile sensor array with a square-shaped acrylic plate or an acrylic plate in the shape of the H letter placed on its top. Their corresponding pressure distributions are shown on the tactile sensor array.

Figure 5a, the index finger is wrapped conformally by the tactile sensor array. The tactile sensor arrays combine the sensing performance of the F-TENG and the flexibility of fabrics. Serving as the warp yarns or weft yarns, the F-TENGs are woven with commercial yarns into the tactile sensor arrays through a shuttle-flying process. F-TENGs are horizontally placed as weft yarns and the other F-TENGs are vertically fixed as warp yarns. Figure 5b demonstrates the schematic of a tactile sensor array with N × N pixels. Each F-TENG is used as an independent electrode, and three common fibers separate the F-TENGs to prevent electrical signals interference between them. Thus, all the electrodes have mutual independent channels. The overlapping region between a weft yarn and a warp yarn constitutes a basic sensing unit of the array with N × N pixels. The overlapping region of weft yarn X_i and warp yarn Y_j is defined as coordinates (X_i and Y_j), where i and j are the serial number of warp yarn and weft yarn, respectively. Figure S16 in the Supporting Information shows the V_{OC}, I_{SC}, and Q_{SC} of a F-TENG that is touched by a finger, which are continuous and replicable. When

the coordinates (X_i, Y_j) are pressed, the corresponding X_i and Y_j channel will have electronic signals simultaneously, which means that the intersections (X_i and Y_j) are touched. Thus, the F-TENG-based tactile sensor arrays can achieve the mapping of external forces.

To further demonstrate the feasibility and repeatability of the F-TENG-based tactile sensor arrays, a tactile sensor array with 8 × 8 pixels is fabricated as a proof-of-concept demonstration, including eight F-TENGs warp yarns and eight F-TENGs weft yarns. As depicted in Figure 5c, when the tactile sensor array is touched, the corresponding pixel of the tactile sensor array will generate output voltage signals. Then, the real-time voltage signals of 16 channels could be detected by the multichannel data acquisition method. Finally, the two signals of a pixel (the two signals from warp yarn and weft yarn, respectively) can be identified, and real-time results can be displayed by the specialized developed data analysis and processing software.

As illustrated in Movie S1 in the Supporting Information, when a finger touches the tactile sensor array, the computer

**ADVANCED
SCIENCE NEWS**
www.advancedsciencenews.com

**ADVANCED
FUNCTIONAL
MATERIALS**
www.afm-journal.de

screen displays the voltage signals and finger touching positions in real time. Through observing the color changes, the touching positions can be recognized (Figure 5d). Therefore, the trajectory of the touching actions can be captured. In addition, the real-time detection of the pressure distribution is a desirable feature. When a square-shaped acrylic plate or an acrylic plate in the shape of the H letter is placed on a tactile sensor array, the pressure distribution can be quickly distinguished, as shown in the Figure 5e and Movies S2–S4 in the Supporting Information. It is necessary to point out that the resolution of the sensor arrays can be conveniently tuned by adjusting the ratio of the F-TENGs to common fibers. The F-TENG-based tactile sensor arrays represent a self-powered, breathable, penetrable, reliable, and comfortable candidate for e-skins, which holds promising applications in pressure tracking and multi-touch devices.

3. Conclusion

In summary, a highly flexible and stretchable coaxial structure F-TENG with the diameter of 0.63 mm is developed by orderly depositing conductive material of Ag NWs/CNT and encapsulated PDMS onto the stretchable spandex fiber. The F-TENG can be stretched over 140% and folded into all kinds of shapes because it is composed of soft and stretchable components. It can also be woven with commercial yarns into a wearable and breathable tactile sensor array. Both the single F-TENG and the tactile sensor arrays can meet the requirements for breathability, permeability, and comfortability. When a piece of Cu film contacts with the F-TENG with the length of 5 cm, the V_{OC} nearly approaches to 22 V. As a self-powered tactile sensor, the F-TENGs can conformally apply on human organs to convert human mechanical energy into electrical signals without affecting the normal movement of human body. A single F-TENG could be used to monitor human motions, such as recording the number of steps, recognizing different gestures of hands, the bending angles of the fingers, etc. In addition, a tactile sensor array with 8 × 8 pixels is developed, through which we can quickly recognize the tactile trajectory and distinguish the real-time pressure distribution.

4. Experimental Section

Materials: The commercial stretchable spandex fiber was chosen as the inner substrate, the nontoxic, harmless, and scalable PDMS was selected as the dielectric material, and CNT/Ag NWs were adopted as the conductive material.

The Preparation of CNT Solution: First, the CNT was melted into pure water to make a solution with a concentration of 0.15%, and 0.03% dodecyl benzenesulfonic acid sodium salt as dispersant was added. Thereafter, these were mixed for 40 min at 800 r min^{-1} by a magnetic stirrer. Finally, the CNT solution was dispersed with an ultrasonic cell grinder for 30 min.

The Fabrication of Conductive Fiber: The conductive ink containing Ag NWs was first deposited on the stretchable spandex fiber substrate. CNT solution was then dip coated onto the resulting fiber through the repeated soaking–drying cycle operation until the CNT covered the surfaces of Ag NWs as well as the gap between them. In the end, the fiber was dried at 50 °C.

The Fabrication of the F-TENGs: First, PDMS was made by mixing the two components in a 1:10 weight ratio. Second, the prepared conductive fibers were vertically fixed in the blast drying oven and PDMS was uniformly coated with a brush at 60 °C. Finally, it was put in the blast drying oven for 30 min until the PDMS was dry and the F-TENGs were formed.

Characterization and Measurement: A Hitachi SU8020 field emission SEM was employed to observe the surface morphology including cross-sectional view of the F-TENG, Ag NW electrode, and CNT electrode. The diameters of the F-TENGs were measured by PARAM CHY-CA thickness tester. Energy dispersive spectroscopy mapping was measured by a Nova Nano SEM 450. The electric outputs of the F-TENGs were measured by a Keithley 6514 electrometer. The multichannel data collection by a NI analog input module and the data processing and analysis software was constructed on the basis of LabVIEW.

Supporting Information

Supporting Information is available from the Wiley Online Library or from the author.

Conflict of Interest

The authors declare no conflict of interest.

[1] F. A. Viola, A. Spanu, P. C. Ricci, A. Bonfiglio, P. Cosseddu, *Sci. Rep.* **2018**, *8*, 8073.

[2] Y. Gao, H. Ota, E. W. Schaler, K. Chen, A. Zhao, W. Gao, H. M. Fahad, Y. Leng, A. Zheng, F. Xiong, C. Zhang, L.-C. Tai, P. Zhao, R. S. Fearing, A. Javey, *Adv. Mater.* **2017**, *29*, 1701985.

[3] S. Gong, W. Schwalb, Y. Wang, Y. Chen, Y. Tang, J. Si, B. Shirinzadeh, W. Cheng, *Nat. Commun.* **2014**, *5*, 3132.

[4] Y. Kim, A. Chortos, W. Xu, Y. Liu, J. Y. Oh, D. Son, J. Kang, A. M. Foudeh, C. Zhu, Y. Lee, S. Niu, J. Liu, R. Pfattner, Z. Bao, T.-W. Lee, *Science* **2018**, *360*, 998.

[5] S. Wang, J. Xu, W. Wang, G. N. Wang, R. Rastak, F. Molina-Lopez, J. W. Chung, S. Niu, V. R. Feig, J. Lopez, T. Lei, S. K. Kwon, Y. Kim, A. M. Foudeh, A. Ehrlich, A. Gasperini, Y. Yun, B. Murmann, J. B. Tok, Z. Bao, *Nature* **2018**, *555*, 83.

[6] J. Cheng, W. Ding, Y. Zi, Y. Lu, L. Ji, F. Liu, C. Wu, Z. L. Wang, *Nat. Commun.* **2018**, *9*, 3733.

[7] K. Dong, Z. Wu, J. Deng, A. C. Wang, H. Zou, C. Chen, D. Hu, B. Gu, B. Sun, Z. L. Wang, *Adv. Mater.* **2018**, *30*, 1804944.

**ADVANCED
SCIENCE NEWS**

www.advancedsciencenews.com

**ADVANCED
FUNCTIONAL
MATERIALS**

www.afm-journal.de

[8] J. Huang, Z. Xu, W. Qiu, F. Chen, Z. Meng, C. Hou, W. Guo, X. Y. Liu, *Adv. Funct. Mater.* **2020**, *30*, 1910547.

[9] Z. Lou, S. Chen, L. Wang, R. Shi, L. Li, K. Jiang, D. Chen, G. Shen, *Nano Energy* **2017**, *38*, 28.

[10] J. C. Yang, J. Mun, S. Y. Kwon, S. Park, Z. Bao, S. Park, *Adv. Mater.* **2019**, *31*, 1970337.

[11] W. W. Lee, Y. J. Tan, H. Yao, S. Li, H. H. See, M. Hon, K. A. Ng, B. Xiong, J. S. Ho, *Sci. Rob.* **2019**, *4*, eaaxeaax2198.

[12] K. Dong, J. Deng, W. Ding, A. C. Wang, P. Wang, C. Cheng, Y.-C. Wang, L. Jin, B. Gu, B. Sun, Z. L. Wang, *Adv. Energy Mater.* **2018**, *8*, 1801114.

[13] Y. Tang, H. Zhou, X. Sun, N. Diao, J. Wang, B. Zhang, C. Qin, E. Liang, Y. Mao, *Adv. Funct. Mater.* **2020**, *30*, 1907893.

[14] J. Zhong, H. Zhu, Q. Zhong, J. Dai, W. Li, S.-H. Jang, Y. Yao, D. Henderson, Q. Hu, L. Hu, J. Zhou, *ACS Nano* **2015**, *9*, 7399.

[15] Z. Li, M. Zhu, J. Shen, Q. Qiu, J. Yu, B. Ding, *Adv. Funct. Mater.* **2020**, *30*, 1908411.

[16] W. Yang, W. Gong, C. Hou, Y. Su, Y. Guo, W. Zhang, Y. Li, Q. Zhang, H. Wang, *Nat. Commun.* **2019**, *10*, 5541.

[17] H. Heidari, *Nat. Electron.* **2018**, *1*, 578.

[18] C. Ning, L. Tian, X. Zhao, S. Xiang, Y. Tang, E. Liang, Y. Mao, *J. Mater. Chem. A* **2018**, *6*, 19143.

[19] E. A. Chapman, P. S. Thomas, E. Stone, C. Lewis, D. H. Yates, *Eur. Respir. J.* **2012**, *40*, 448.

[20] A. Miyamoto, S. Lee, N. F. Cooray, S. Lee, M. Mori, N. Matsuhisa, H. Jin, L. Yoda, T. Yokota, A. Itoh, M. Sekino, H. Kawasaki, T. Ebihara, M. Amagai, T. Someya, *Nat. Nanotechnol.* **2017**, *12*, 907.

[21] K. Dong, X. Peng, J. An, A. C. Wang, J. Luo, B. Sun, J. Wang, Z. L. Wang, *Nat. Commun.* **2020**, *11*, 2868.

[22] X. Peng, K. Dong, C. Ye, Y. Jiang, S. Zhai, R. Cheng, D. Liu, G. Xiaoping, J. Wang, Z. L. Wang, *Sci. Adv.* **2020**, *6*, eabaeaba9624.

[23] F.-R. Fan, Z.-Q. Tian, Z. L. Wang, *Nano Energy* **2012**, *1*, 328.

[24] Y. Mao, P. Zhao, G. McConohy, H. Yang, Y. Tong, X. Wang, *Adv. Energy Mater.* **2014**, *4*, 1301624.

[25] Y. Zi, S. Niu, J. Wang, Z. Wen, W. Tang, Z. L. Wang, *Nat. Commun.* **2015**, *6*, 8376.

[26] K. Dong, J. Deng, Y. Zi, Y. C. Wang, C. Xu, H. Zou, W. Ding, Y. Dai, B. Gu, B. Sun, Z. L. Wang, *Adv. Mater.* **2017**, *29*, 1702648.

[27] J. Luo, Z. Wang, L. Xu, A. C. Wang, K. Han, T. Jiang, Q. Lai, Y. Bai, W. Tang, F. R. Fan, Z. L. Wang, *Nat. Commun.* **2019**, *10*, 5147.

[28] C. Zhang, Z. Guo, X. Zheng, X. Zhao, H. Wang, F. Liang, S. Guan, Y. Wang, Y. Zhao, A. Chen, G. Zhu, Z. L. Wang, *Adv. Mater.* **2020**, *32*, 1904988.

[29] Y. Zhou, C.-H. Wang, W. Lu, L. Dai, *Adv. Mater.* **2020**, *32*, 1902779.

[30] G. Qu, J. Cheng, X. Li, D. Yuan, P. Chen, X. Chen, B. Wang, H. Peng, *Adv. Mater.* **2016**, *28*, 3646.

[31] H. Sun, Y. Zhang, J. Zhang, X. Sun, H. Peng, *Nat. Rev. Mater.* **2017**, *2*, 17023.

[32] Y. Zhang, L. Wang, Z. Guo, Y. Xu, Y. Wang, H. Peng, *Angew. Chem., Int. Ed. Engl.* **2016**, *55*, 4487.

[33] X. Xu, S. Xie, Y. Zhang, H. Peng, *Angew. Chem., Int. Ed. Engl.* **2019**, *58*, 13643.

[34] M. Hatamvand, E. Kamrani, M. Lira-Cantú, M. Madsen, B. R. Patil, P. Vivo, M. S. Mehmood, A. Numan, I. Ahmed, Y. Zhan, *Nano Energy* **2020**, *71*, 104609.

[35] X. Chen, L. Qiu, J. Ren, G. Guan, H. Lin, Z. Zhang, P. Chen, Y. Wang, H. Peng, *Adv. Mater.* **2013**, *25*, 6436.

[36] M. Liu, X. Pu, C. Jiang, T. Liu, X. Huang, L. Chen, C. Du, J. Sun, W. Hu, Z. L. Wang, *Adv. Mater.* **2017**, *29*, 1703700.

[37] S. Honda, Q. Zhu, S. Satoh, T. Arie, S. Akita, K. Takei, *Adv. Funct. Mater.* **2019**, *29*, 1807957.

[38] K. Dong, X. Peng, Z. L. Wang, *Adv. Mater.* **2019**, *32*, e1902549.

[39] Z. L. Wang, *Nano Energy* **2020**, *68*, 104272.

[40] J. Wang, M.-F. Lin, S. Park, P. S. Lee, *Mater. Today* **2018**, *21*, 508.

[41] S. Liu, Y. Li, W. Guo, X. Huang, L. Xu, Y.-C. Lai, C. Zhang, H. Wu, *Nano Energy* **2019**, *65*, 104005.